Structural, Mechanical and Thermal Studies of Double-Molded Isotactic Polypropylene Nanocomposites with Multiwalled Carbon Nanotubes

Md. Forhad Mina,[1] Md. Akramul Haque,[1] Md. Khairul Hassan Bhuiyan,[2] Md. Abdul Gafur,[3] Yukihiro Tamba,[4] Tsutomu Asano[5]

[1]*Department of Physics, Bangladesh University of Engineering and Technology, Dhaka 1000, Bangladesh*
[2]*Department of Physics and Chemistry, Faculty of Agriculture, Bangladesh Agricultural University, Mymensingh 2202, Bangladesh*
[3]*PP & PDC, Bangladesh Council of Scientific and Industrial Research, Dhaka 1205, Bangladesh*
[4]*General Education, Suzuka National College of Technology, Suzuka 510-0294, Japan*
[5]*Center for Instrumental Analysis, Shizuoka University, Shizuoka 422-8529, Japan*

Received 22 October 2009; accepted 24 February 2010
DOI 10.1002/app.32354
Published online 19 May 2010 in Wiley InterScience (www.interscience.wiley.com).

ABSTRACT: Nanocomposites of isotactic polypropylene (iPP) and multiwalled carbon nanotubes (MWCNTs) with various contents of MWCNTs were fabricated by double molding techniques. X-ray diffraction measurements reveal a development of α-crystal with lamellar stacks having a long period of 150 Å in the neat iPP that increases to 165 Å in 2 wt % MWCNTs-loaded composites, indicating that MWCNTs enhance crystallization of iPP as a nucleating factor. Mechanical properties, such as tensile strength, flexural strength, Young's modulus, tangent modulus, and microhardness are found to increase with increasing MWCNTs content. Thermal analyses represent an increase of crystallization and melting temperatures and a decrease of thermal stability of the composites with increasing MWCNTs. Changes in structural, mechanical, and thermal properties of the composites due to the addition of MWCNTs are elaborately discussed. © 2010 Wiley Periodicals, Inc. J Appl Polym Sci 118: 312–319, 2010

Key words: nanocomposites; polypropylene (PP); x-ray; mechanical properties; thermal properties

INTRODUCTION

A wide choice of nanoscaled organic/inorganic fillers, such as carbon nanotubes (CNTs), carbon nanofibers, fullerenes, clay, talc, titanium dioxide, etc. are mixed up with polymers to produce new substances with desired properties. Among them, CNTs have stimulated much interest recently as they have emerged as potentially ideal reinforcement for producing nanocomposites with unique physical properties.[1–4] Owing to extraordinarily high Young's modulus, strength, and resilience of CNTs, reports on the mechanical properties of polymer/CNTs composites considerably increased in the last 5 years.[4–11] In addition, CNTs have a large aspect ratio, low density, and are short enough to allow moldings of complex shapes.[12–14]

Among the most versatile polymers, isotactic polypropylene (iPP) is very widely used in composite fabrication because of their good balance between properties and cost, as well as their nice processability and low density. However, the mechanical and thermal properties of iPP are sometimes not sufficient for applications as engineering plastics. Therefore, iPP is generally modified with nanoscaled clay and fibers.[13–16] Recently, CNTs are also used as special nanofiller to prepare iPP/CNTs composites, providing a new avenue of fabricating high performance iPP engineering plastics.[17–20]

The structure of CNTs can be single walled (SWCNTs) or multiwalled (MWCNTs) of which the latter is simply composed of concentric single-walled nanotubes having more rigid structure than the former one. The diameter of single-walled carbon nanotubes ranges from one up to a few nanometers and their length is a few micrometer. The small size of the nanotubes ensures a good surface finish and the high aspect ratio allows electrical percolation at very low loading of CNTs in polymers. Besides, the crystalline quality of the carbon results in a high conductivity and excellent mechanical properties as compared with the conventional carbon black. Despite the promising potential of CNTs, difficulties have been encountered in exploiting many impressive fundamental properties like temperature resistance, crystallinity, nanostructure, thermal expansion coefficient, dielectric constant, and so on due to the irregular dispersal of the CNTs within polymer matrix.[12,21] On the other hand, outstanding mechanical

Correspondence to: Md. F. Mina (mfmina@phy.buet.ac.bd).
Contract grant sponsor: Bangladesh University of Engineering and Technology (BUET).

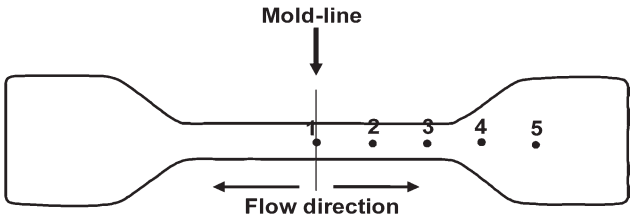

Figure 1 Schematic diagram of the sample–die or the sample–shape. iPP-MWCNTs melt mixtures are injected along the mold line, flowing along the indicated direction into the die. Successive positions 1, 2, 3, 4, and 5 on the sample are 1 cm apart.

properties of MWCNTs are of little value unless they can be successfully incorporated into a matrix.

Considering the above facts, we prepared iPP/MWCNTs composites by well mixing the MWCNTs with the iPP matrix through multiple extrusions, followed by injection molding. The aim of this work is to study the effect of nanotube content on structural, mechanical, and thermal properties of the composites of iPP and MWCNTs.

EXPERIMENTAL

Sample preparation

Composites were prepared from granular-shaped iPP (molecular weight, M_w = 184,700 g mol^{-1}) with MWCNTs. Commercial grade iPP was purchased from BASF, Germany and MWCNTs powder was collected from Shenzben Nanotech Port Co., China (L.MWNTs-1030). The diameter and length of MWCNTs have the range 10–30 nm and 5–15 μm, respectively. MWCNTs powder was mixed in iPP with appropriate ratios. A neat iPP sample and the separate mixtures of iPP and MWCNTs with 0.01, 0.05, 0.10, 0.50, 1.0, and 2.0 wt % MWCNTs content were molded thrice by an extruder machine (Axon AB, Sweden). The extruder has five heating zones with blending temperature profiles of 180, 185, 190, 195, and 200°C. During preparation of samples, the screw rotating speed was 100 rpm. The molten extrudates were pressed and cooled to obtain flat-shaped solid sample. The solid samples were cut into pieces, which were again molded in a dumbbell-shaped die by a locally fabricated injection molding machine.

Figure 1 indicates a scheme of the sample die, which is the same as that of the sample shape and shows a mold line along which the molten extrudates were injected into the die. The flow direction of the melt into the die is also indicated. On the sample surface (Fig. 1), marks 1, 2, 3, 4, and 5 are given from the mold line towards flow direction. Each successive mark is 1 cm apart. The melt flow is first disturbed at position 1 during injection and again disturbed at positions 4 and 5 due to the widened width of the dumbbell. After the injection, the molten extrudates are crystallized during cooling at ambient condition. The crystallization of the sample commences from both end of the dumbbell, following the direction from positions 5 to 1. The solid samples were subjected to measure structure and properties by the following experiments.

X-ray diffraction measurements

Simultaneous wide-angle and small-angle X-ray scattering (WAXS and SAXS) measurements of the samples were performed using a rotating anode type high intensity Rotaflex, RU-300 X-ray generator (40 kV × 200 mA; Rigaku Corporation Tokyo, Japan). The incident X-ray beam, monochromatized by a graphite single crystal, had a wavelength of 1.54 Å. The X-ray beam was passed through a collimation system with a pinhole 100 μm in diameter. The camera lengths for WAXS and SAXS were fixed at 46 and 460 mm, respectively. The diffraction intensity was recorded by a Rigaku Display System imaging plate (IP) (Rigaku Corporation, Tokyo, Japan). The exposure time was set as 60 min in every X-ray measurements.

Both the WAXS and SAXS measurements of the neat iPP and 2.0 wt % MWCNTs-loaded iPP were carried out at different positions 1–5 (Fig. 1) of the sample. The WAXS and SAXS measurements were also performed at position 2 of all 0–2.0 wt % MWCNTs-loaded samples.

Mechanical testing

Tensile strength (TS), percentage of elongation-at-break [EB(%)] and Young's modulus (Y) of the samples were measured by a universal testing machine [Hounsfield UTM 10KN; ASTM D-638−98] at a crosshead speed of 0.001 m min^{-1}, keeping a gauge length of 0.06 m. Flexural strength, (FS), flexural strain [FB(%)], and tangent modulus (G) were also measured by the same apparatus, keeping a distance of 0.064 m between two supports on which the samples were placed to employ load. Five samples of each composition were used in the mechanical testing.

Micromechanical testing

A software controlled Vicker's square-based diamond indenter (Shimadzu, Japan) was employed to measure the microhardness (H) from the residual impression on the sample surface after an indentation time of 6 s. Loads of 0.098, 0.245, 0.490, and 0.980 N were used to derive a load independent value of H in MPa by the following relation:[22]

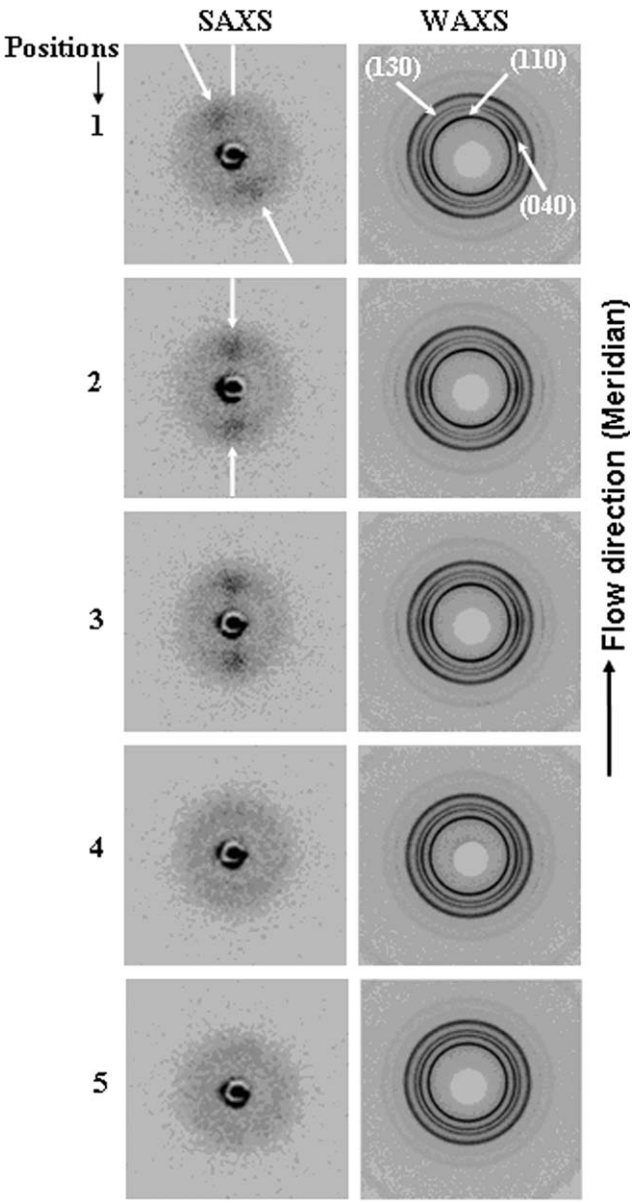

Figure 2 Simultaneous SAXS and WAXS photographs taken at positions 1–5 of the neat iPP sample. Meridian is parallel to the flow direction. White arrows indicate reflections from planes of the lamellae.

$$H = K\frac{P}{d^2} \tag{1}$$

where d (m) is the length of indentation diagonal, P (N) the applied load, and K a geometrical factor equal to 1.854. Samples with flat and smooth surface immediately after their preparation were used for this measurement. At least eight imprints were taken on the sample surface for each load, and the H was evaluated from the average value of all impressions.

Indentations were also taken at different positions from 1 to 4 (Fig. 1) on the sample surface at an interval of 0.5 cm from the mold line down the flow direction. To have an average position-dependent hardness value, at least five indentations were taken on a straight line along the width for each position. From these indentations, average diagonal lengths, d_{hor} along the flow direction, and d_{per} along the perpendicular to the flow direction, were also measured for each position. From the values of d_{hor} and d_{per}, H_{hor} and H_{per} were evaluated, respectively. Then the indentation anisotropy (ΔH) was evaluated by the following formula.[22]

$$\Delta H = 1 - (H_{hor}/H_{per}) \tag{2}$$

Thermal measurements

Thermal properties of the samples were monitored by a coupled differential thermal analyzer (DTA) and thermogravimetric analyzer (TGA) [Seiko-Ex-STAR-6300, Japan]. The measurements using DTA and TGA were carried out from room temperature) (37°C) to 600°C at a heating rate of 20°C min^{-1} under nitrogen gas flow. While the DTA traces give the crystallization, melting, and degradation temperatures as determined from the exotherm versus temperature curves, the TGA runs exhibit the weight loss of the sample with temperature.

RESULTS AND DISCUSSION

Structural analysis

Figure 2 shows SAXS and WAXS photographs at positions 1–5 of the neat iPP sample. Here, the meridian is parallel to the flow direction. Analysis of SAXS results indicates that the long period of lamellar stacks is about 150 Å in the neat iPP. WAXS reflections are indexed as 110, 040, and 130, representing α-crystal of iPP.[23–25] At position 1, the SAXS two-point reflections (indicated by arrows) are inclined at an angle of about 25° from the meridian, implying that the lamellae are inclined due to disturbance of the melt flow. SAXS reflections for positions 2 and 3 are strong on the meridian. WAXS patterns of positions 2 and 3 also indicate that 110 arc pattern is slightly stronger on the meridian, whereas 040 arc is located around the equator. For positions 4 and 5, two-point patterns of SAXS disappear and the WAXS photograph does not show any arc-like reflection. This result suggests that the crystalline and lamellar orientation disappear at positions 4 and 5.

Figure 3 illustrates SAXS and WAXS photographs at positions 1–5 of the 2.0 wt % MWCNTs-loaded iPP. For position 1, the SAXS reflection is inclined by about 45° with the meridian due to the flow disturbance. On the other hand, the SAXS peaks are located on the meridian for positions 2 and 3. Therefore lamellar and crystalline orientation is analyzed to be nearly the same structure as that observed in

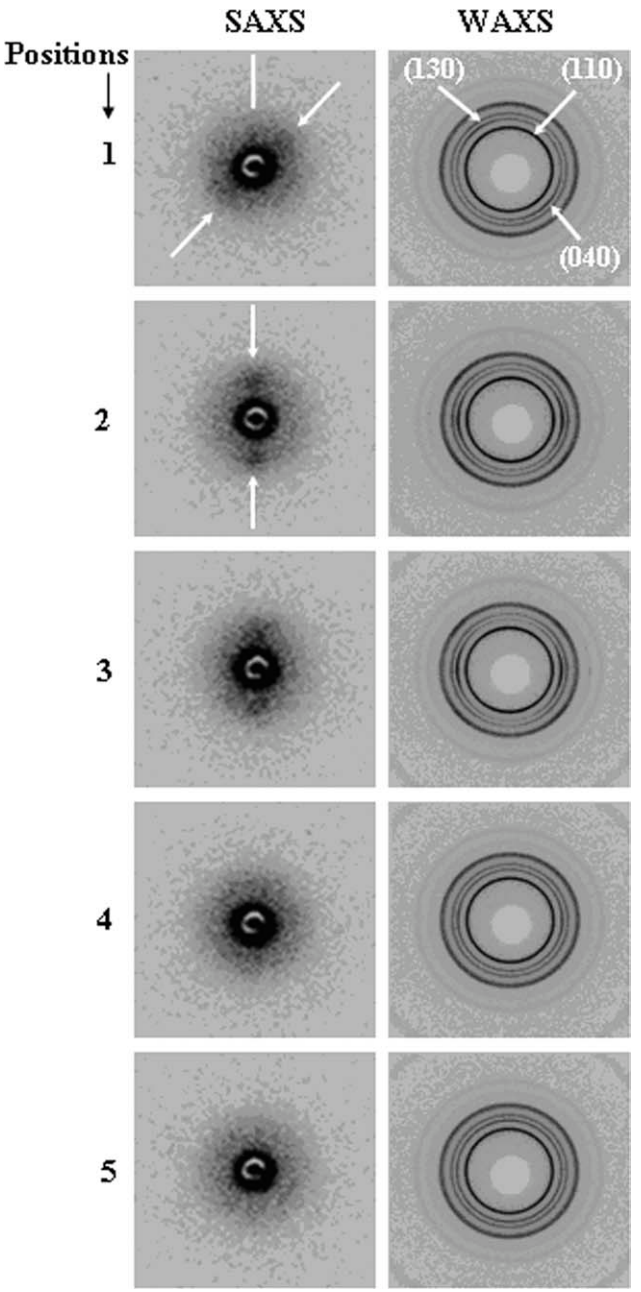

Figure 3 Simultaneous SAXS and WAXS photographs taken at positions 1–5 of the 2.0 wt % MWCNTs-loaded composite.

the neat iPP. Comparing the SAXS patterns in Figures 2 and 3, the peak position is slightly shifted to inner angle in Figure 3, indicating that the long period of lamellar stacks increases to 165 Å. Besides, new reflection also appears near the center of SAXS photographs. This SAXS reflection can possibly be attributed to the presence of MWCNTs aggregates. The angle of this new reflection is about half of that of the lamellar reflection. Thus, the average size of the MWCNT aggregates is estimated to be larger than 330 Å. For positions 4 and 5, both SAXS and WAXS photographs show circular patterns indicating lack of orientation as that observed in the case of the neat iPP.

MWCNTs have often been reported to have an orienting effect on the polymer matrix.[26,27] In this study, however, no significant difference in orientation is found between iPP and the composites. This lack of strong orientating effect is in agreement with published report.[28]

Figure 4 represents SAXS and WAXS photographs of the neat iPP and the composites taken at position 2. The SAXS intensity of the central reflection increases with the addition of MWCNTs content. The SAXS reflection on the meridian moves slightly towards inner angle with loading of MWCNTs content, showing that the long period of lamellar stacks increases from 150 to 165 Å. This fact strongly

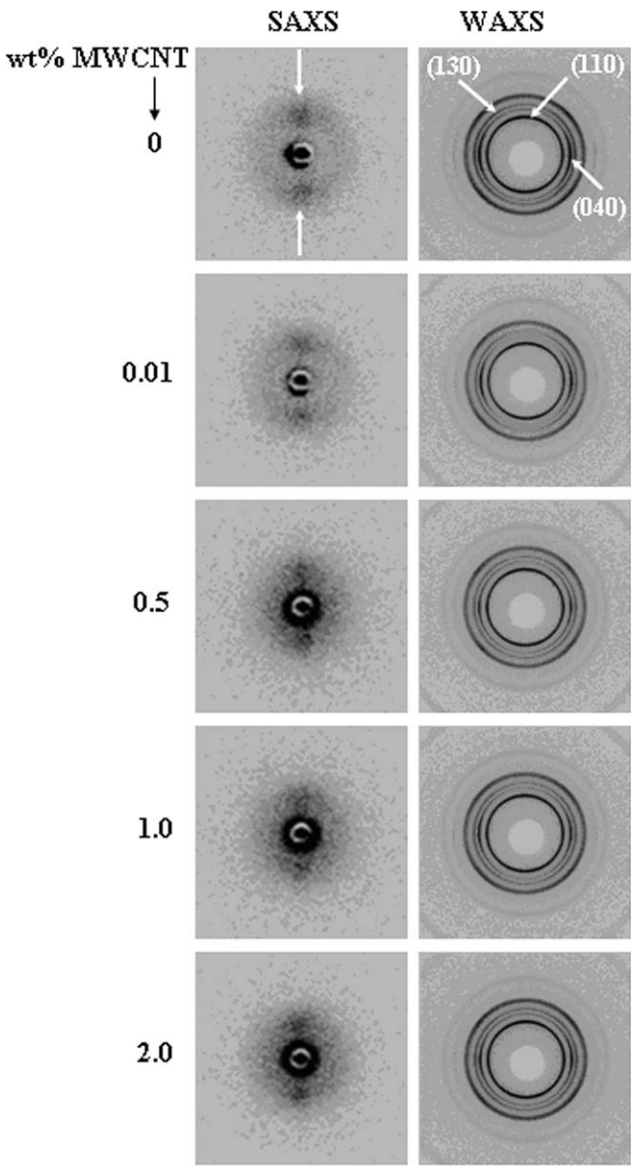

Figure 4 Simultaneous SAXS and WAXS photographs of the 0, 0.01, 0.5, 1.0, and 2.0 wt % MWCNTs-loaded samples taken at position 2.

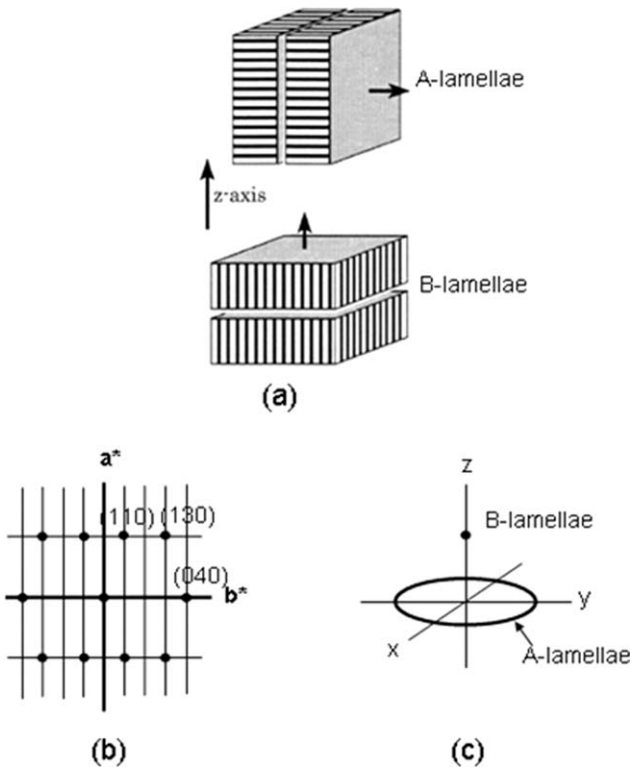

Figure 5 (a) Schematic definitions of A- and B-lamellae, (b) Reciprocal lattice points of the α-crystal on a^*b^*-plane and (c) Description of expected SAXS reflections of A- and B-lamellae, where x, y, and z axes are parallel to the direction of thickness, width and flow direction of the sample.

indicates that the nanotube content enhances crystallization of iPP. It is possible to consider that the MWCNTs aggregates will contribute to act as a heterogeneous nucleating agent. On the other hand, arc-like reflections of WAXS remain unchanged with the increase of the filler content (Fig. 4), showing that iPP crystal is unaffected by MWCNTs. A number of authors have reported that the influence of nanofillers on the structure and morphology is exerted at a lamellar level rather than at a crystalline cell level.[29–31] Therefore, SAXS is only sensitive to the crystalline regions organized in lamellar stacks, whereas WAXS allows detection of all regions contributing to the semicrystalline framework, including the amorphous phase located between the lamellar stacks.

To analyze spherulitic crystallization, we define A- or B-lamellae whose normals are respectively perpendicular or parallel to the growth direction as shown in Figure 5(a). Here, the lamellar spacing includes both crystalline and amorphous thickness. In the α-spherulite, A-lamellae are first developed along the growth direction, where the molecular c-axis is oriented perpendicular to it and are known to have a*-orientation.[23–25] In this case, 110 reflection appears near the meridian, whereas 040 reflection is located on the equator as illustrated in Figure 5(b). Due to the helical conformation of α-iPP molecule, the crosshatched B-lamellae are epitaxially grown on the (010) plane of A-lamellae.[23–25] The c-axis of B-lamellae is then oriented parallel to the growth direction, where the (010) plane is parallel to that of A-lamellae.

According to Figure 5(a), the SAXS reflections of A- and B-lamellae will appear on the equator and meridian, respectively. We define x, y, and z axes parallel to the direction of thickness, width, and flow direction of the dumbbell-shaped sample as indicated in Figure 5(c). If we consider uniaxial growth along z-axis (sharp orientation of the flow direction), we have so-called four-point patterns, where the reflection of A-lamellae will appear on the equator, whereas that of B-lamellae will concentrate on the meridian. In the case of fluctuation (disturbance) of the flow direction, the equatorial (A-lamellar) reflection is soon weakened and meridional (B-lamellar) reflection remains by Lorentz's factor.

In the WAXS patterns in Figure 4, the 040 reflection is oriented on the equator. This fact is explained by the common (010) epitaxial plane in A- and B-lamellae. The orientation of the common plane is emphasized when the 110 and 130 reflections are distributed due to the fluctuation of the flow direction. Thus, the most probable structure of the injected samples is a*-oriented A-lamellae grown along the flow direction and epitaxial B-lamellae. The crystallization is enhanced by the incorporation of MWCNTs granules.

Mechanical and micromechanical properties

Figure 6 illustrates the variations of TS and EB (%) with MWCNTs content. The TS value is lower and the EB (%) value is higher for the neat iPP sample as compared to that for the composites. Although the

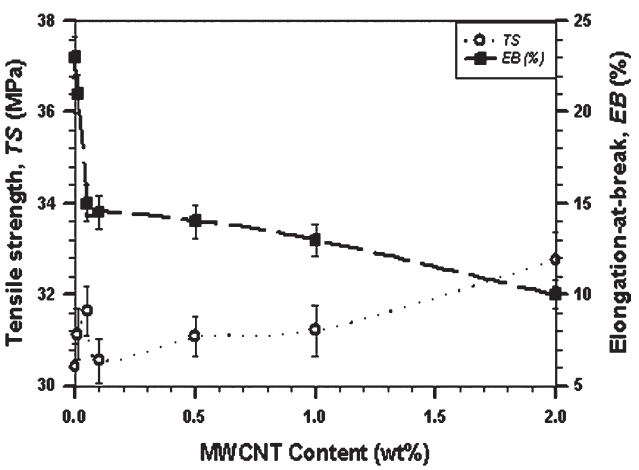

Figure 6 Variation of tensile strength (TS) and elongation-at-break [EB (%)] of the nanocomposites with various content of MWCNTs.

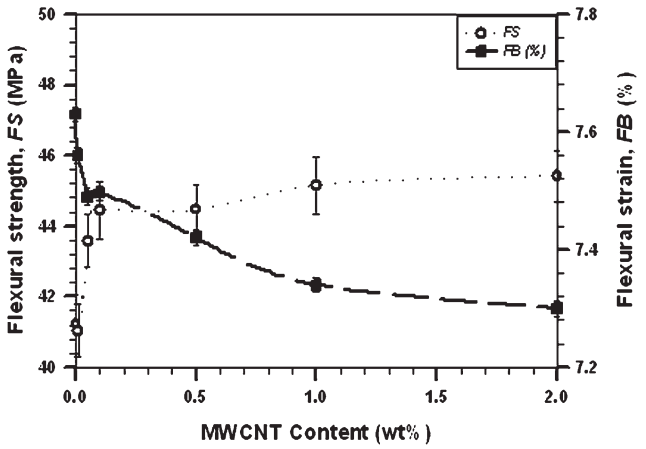

Figure 7 Variation of flexural strength (FS) and percentage of flexural strain [FB(%)] of the nanocomposites with various content of MWCNTs.

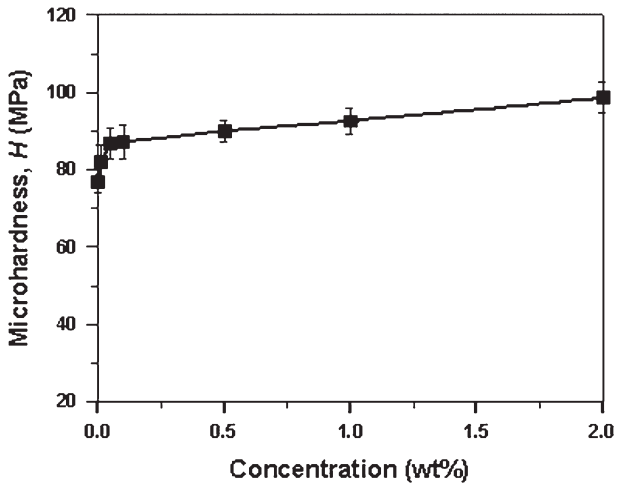

Figure 9 Change of microhardness with MWCNTs concentrations.

TS value is seen to increase with filler content, the *EB* (%) shows rapid decrease with small content less than 0.1 wt % of MWCNTs. Almost similar results are observed in the findings of FS and FB(%) (Fig. 7). *Y* and *G* shows an increase with the increase of filler content as presented in Figure 8.

These mechanical results indicate that stiffness of the composite increases, while brittleness appears with MWCNTs. Filler-loaded samples show increased crystallinity, as obvious from the X-ray results. The thicker lamellae promote TS, *Y*, and *G* values. On the other hand, the neat iPP sample has more amorphous regions. On the mechanical deformation, the long polymer chain can easily be deformed in the amorphous regions. Thus, the neat iPP sample can show higher EB(%) than the composites.

Figure 9 shows the variation of *H* with respect to MWCNTs content. The *H* value of the neat iPP sample is observed to be about 75 MPa. The *H* increases gradually with the increase of MWCNTs content. In case of indentation measurements, both elastic and plastic deformations occur in the sample for the application of a load. Removal of the load causes a residual impression on the sample surface that exists due to the plastic deformation in the material. Therefore, if defects would grow in the samples, they would generally result in higher diagonal length that corresponds to lower microhardness value. However, observed results show a higher *H* value with the increase of nanotube. This increase of *H* clarifies good interfacial adhesion between filler and polymer.

Figure 10 represents the *H* and ΔH changes with respect to distance of the 0.5 wt % MWCNTs-loaded sample as measured from the mold line down the flow direction. Here, 0, 1, 2, and 3 cm correspond to the positions 1, 2, 3, and 4 of Figure 1. Two different microhardness values, H_{hor} and H_{per} arise due to the

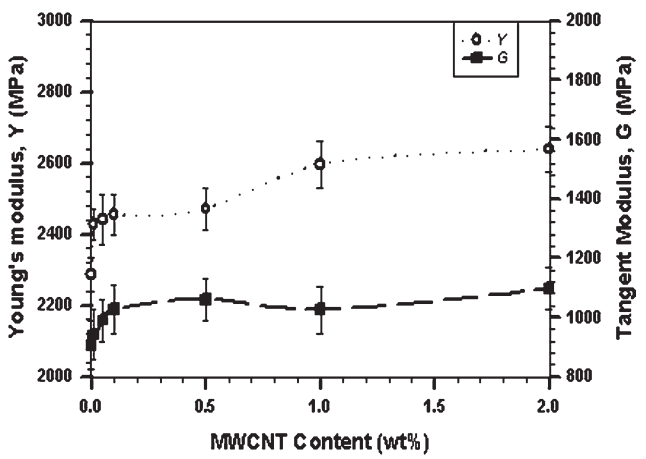

Figure 8 Dependence of Young's modulus (*Y*) and tangent modulus (*G*) of the nanocomposites with various content of MWCNTs.

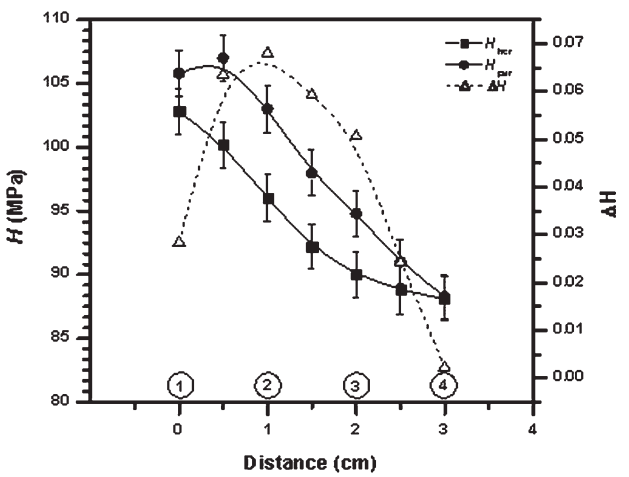

Figure 10 Position-dependent microhardness (H_{hor} and H_{per}) and hardness anisotropy (ΔH) measured from positions 1 to 4 at an interval of 0.5 cm. H_{hor} and H_{per} are hardness values parallel and perpendicular to the flow direction.

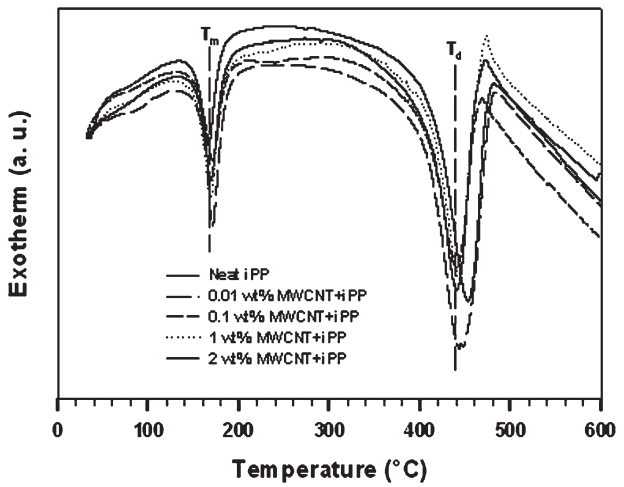

Figure 11 DTA thermograms of the neat iPP and nanocomposites of 0.01, 0.1, 1.0, and 2.0 wt % MWCNTs content.

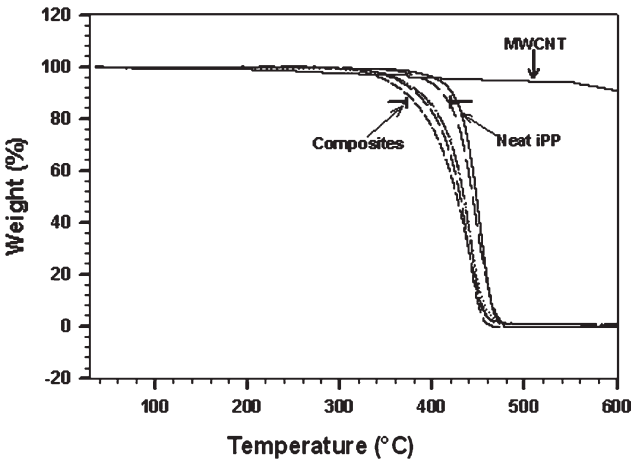

Figure 13 TGA thermograms of the neat iPP (solid line), MWCNT (solid line) and nanocomposites of 0.01, 0.1, 1.0, and 2.0 wt % MWCNTs (dashed curves in arrow lines: ⊣⊢).

anisotropy of indentation on sample surface. The more the difference between the values of H_{hor} and H_{per}, the greater is the anisotropy. Clearly, the hardness anisotropy ΔH increases and becomes maximum at position 2 after which it decreases. These results agree with the crystal structure obtained by SAXS and WAXS at positions 2 and 3.

Thermal properties

The DTA thermograms of the iPP sample and the composites containing various amounts of MWCNTs are presented in Figure 11. Each DTA run of the samples investigated shows two peaks that respectively represent a sharp melting temperature (T_m) at around 165°C and a sharp thermal degradation temperature (T_d) at around 450°C. The change of T_m for various MWCNTs content is highlighted in Figure 12, showing an increase of T_m with the increase of filler. To explain this result, we invoke the relation of melting temperature, T_m, of a laterally grown large lamellar crystal as described by the simplified Thomson–Gibbs equation:[32]

$$T_m = T_m^0 \left(1 - \frac{2\gamma}{l\Delta h_f'}\right) \quad (3)$$

where T_m^0 is the melting temperature of the infinitely large crystal, γ the top and bottom specific surface free energy, l the lamellar thickness and $\Delta h_f'$ the bulk heat of fusion per cubic centimeter. Clearly, T_m increases if the thickness of the lamella increases. Thus, MWCNTs act as additional active substrates, promoting thicker lamella of iPP matrix. This fact is in good agreement with that of SAXS in Figure 3.

The TGA curves as shown in Figure 13 exhibit the weight loss of the samples with increasing temperature. Solid-lines show the weight loss of the neat iPP and MWCNTs, whereas the dashed-lines enclosed by arrow-lines (⊣⊢) indicate the weight loss by the composites. The weight decrease basically starts from 200°C and the actual onset of weight loss, i.e. the sharp fall of TGA curve with respect to MWCNTs content, is found to be decreasing with the addition of filler. However, it is a common practice to consider the degradation temperature at 50% weight loss of the sample as an indicator for structural destabilization.[33,34] Analysis shows that the neat iPP sample is seen to be thermally stable up to 445°C, whereas the 2.0 wt % MWCNTs-loaded sample shows the maximum thermal stability at about 424°C. In the composites, MWCNTs probably locate in interfacial region between spherulite. In this case, the filler makes brittleness as observed in the early stage of EB(%) and enhances degradation during heating. The high heat capacity and thermal

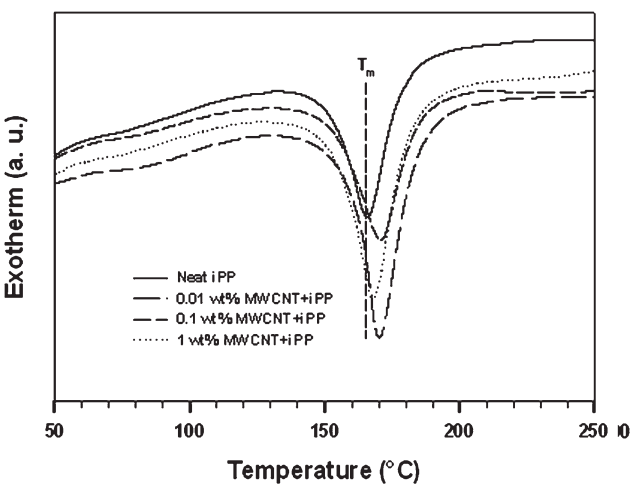

Figure 12 Enlarged DTA thermograms of Figure 11.

conductivity of MWCNTs then causes them to quickly reach a higher temperature than the surrounding matrix. This will cause degradation of the composites at a lower temperature.

However, considering the observed increase of TS, FS, FB(%), Y, H, T_m, and T_d with increasing filler along with X-ray results, we suggest that the adhesion between filler and matrix is good. A hypothesis can be put forth regarding TS and EB(%) values for the composites: Due to the restriction to chain mobility in the composites, the stress may be concentrated at the filler–polymer interface, which may develop local crazes and cracks that quickly propagate in three directions, resulting in sample's fracture relatively at high TS and low EB(%). In this investigation, a good adhesion between filler and iPP is attained by fabricating the composites through double molding methods using an extruder and an injection molding machine, and the multiwalled carbon nanotubes have a considerable influence on the structural, mechanical, and thermal properties of the nanocomposites.

CONCLUSIONS

A good adhesion between multiwalled carbon nanotubes and polymer matrix in the iPP/MWCNTs composites is achieved by double molding techniques employed successively by an extrusion and an injection molding machines. Molecular orientation near the mold line, change of lamellar period and increased crystallinity with the inclusion of MWCNTs contents in iPP are observed by X-ray diffraction studies. Improved tensile strength, flexural strength, Young's modulus, tangent modulus, and microhardness values as well as enhanced melting temperatures of composites with increasing MWCNTs contents are also observed. These results indicate a good adhesion between filler and polymer matrix, showing better performances of the composites.

The authors are grateful to the Department of Materials and Metallurgical Engineering, BUET and Bangladesh Council of Scientific and Industrial Research (BCSIR) to allow facilities for this research. The research was partially carried out at the Center for the Instrumental Analysis, Shizuoka University, Japan.

References

1. Liu, X.; Wu, Q.; Berglund, L. A.; Fan, J.; Qi, Z. Polymer 2001, 42, 8235.
2. Park, Ch. I.; Park, O. Ok.; Lim, J. G.; Kim, H. J. Polymer 2001, 42, 7465.
3. Sandler, J.; Shaffer, M. S. P.; Prasse, T.; Bauhofer, W.; Schulte, K.; Windle, A. H. Polymer 1999, 40, 5967.
4. Jin, Z.; Pramoda, K. P.; Xu, G.; Goh, S. H. Chem Phys Lett 2001, 337, 43.
5. Cooper, C. A.; Ravich, D.; Lips, D.; Mayer, J.; Wagner, H. D. Compos Sci Technol 2002, 62, 1105.
6. Tang, W.; Santare, M. H.; Advani, S. G. Carbon 2003, 41, 2779.
7. Roslaniec, Z.; Broza, G.; Schulte, K. Compos Interface 2003, 10, 95.
8. Gorga, R. E.; Cohen, R. E. J Polym Sci Part B: Polym Phys 2004, 42, 2690.
9. Clayton, L. M.; Gerasimov, T. G.; Cinke, M.; Meyyappan, M.; Harmon, J. P. Polym Bull 2004, 52, 259.
10. Calvert, P. Nature 1999, 399, 210.
11. Salvetat, J. P.; Briggs, G. A. D.; Bonard, J. M.; Bacsa, R. R.; Kulik, A. J.; Strockli, T.; Burnham, N. A.; Forro, L. Phys Rev Lett 1999, 82, 944.
12. Subramoney, S. Adv Mater 1998, 10, 1157.
13. Kawasumi, M.; Hasegawa, N.; Kato, M.; Usuki, A.; Okada, A. Macromolecules 1997, 30, 6333.
14. Li, J.; Zhou, C. X.; Wang, G.; Zhao, D. L. J Appl Polym Sci 2003, 89, 3609.
15. Wu, C. M.; Chen, M.; Karger-Kocsis, J. Polym Bull 1998, 41, 493.
16. Assouline, E.; Pohl, S.; Fulchiron, R.; Gerard, J. F.; Lustigar, A.; Wagner, H. D.; Marom, G. Polymer 2000, 21, 7843.
17. Zhou, Z.; Wang, S. F.; Lu, L.; Zhang, Y.; Zhang, Y. X. J Polym Sci Part B: Polym Phys 2007, 45, 1616.
18. Zhao, P.; Wang, K.; Yang, H.; Zhang, Q.; Du, R. N.; Fu, Q. Polymer 2007, 48, 5688.
19. Jose, M. V.; Dean, D.; Tyner, J.; Price, G.; Nyairo, E. J Appl Polym Sci 2007, 103, 3844.
20. Alig, I.; Lellinger, D.; Dudkin, S. M.; Potschke, P. Polymer 2007, 48, 1020.
21. Barber, A. H.; Cohen, S. R.; Wagner, H. D. Appl Phys Lett 2003, 82, 4140.
22. Balta Calleja, F. J.; Fakirov, S. Microhardness of Polymers; Cambridge University Press: United Kingdom, 2000.
23. Asano, T.; Mina, Md. F.; Fujiwara, Y. A Survey of Polymer Crystallization by X-ray Diffraction; SKP Inc: Shizuoka, Japan, 2006; Chapter 5, p 48–55.
24. Asano, T.; Fujiwara, Y. Polymer 1978, 19, 99.
25. Asano, T.; Imaizumi, K.; Tohyama, N.; Yoshida, S. J Macromol Sci Phys 2004, 43, 639.
26. Tabunai, D.; Granelli, W.; Camino, G.; Class, M. e-Polymers 2007, 1.
27. Hou, Z.; Wang, K.; Zhao, P.; Zhang, Q.; Yang, C.; Chen, D.; Du, R.; Fu, Q. Polymer 2008, 49, 3582.
28. Causin, V.; Yang, B.-X.; Marega, C.; Goh, S. H.; Marigo, A. Eur Polym J 2009, 45, 2155.
29. Maiti, P.; Hoai Nam, P.; Okamoto, M. Macromol 2002, 35, 2042.
30. Truss, R. W.; Yeow, T. K. J Appl Polym Sci 2006, 100, 3044.
31. Causin, V.; Yang, B.-X.; Marega, C.; Goh, S. H.; Marigo, A. J Nanosci Nanotechnol 2008, 8, 1790.
32. Wunderlich, B. Macromolecular Physics; Academic Press: 1980; Vol. 3: p 30.
33. Kumer, R. V.; Koltypin, Y.; Gedanken, A. J Appl Polym Sci 2002, 86, 160.
34. Kumer, R. V.; Koltypin, Y.; Palchik, O.; Cohen, Y. S.; Cohen, Y.; Aurbach, D.; Palchik, O.; Felner, I. J Mater Chem 2000, 10, 1125.